Università degli Studi di Padova

Department of Information Engineering

Master Thesis in ICT for Internet and Multimedia

A.Y. 2018/2019

Laser Trimming of Silicon Nitride Racetrack Resonators

Supervisor
Luca Palmieri
Università di Padova

Master Candidate
Greta De Paoli

Co-supervisors
Frederic Y. Gardes
University of Southampton

Milan Milosevic
University of Southampton

Date: 09/12/2019

Abstract

A novel technique for trimming the resonance wavelength of nitrogen-rich silicon nitride racetrack resonators is presented.
A portion of the ring is exposed to a UV laser beam (244 nm) and a shift of the operating wavelength is then observed.
Linear dependence of the shift on the length of the exposed portion has been proven, as well as the possibility of covering an entire FSR.
This technique can be applied to both devices with and without a silicon dioxide top cladding.

Contents

ABSTRACT v

LIST OF FIGURES xi

LIST OF TABLES xiii

1 INTRODUCTION 3
- 1.1 Silicon Photonics 3
  - 1.1.1 History of Silicon Photonics 3
- 1.2 Silicon Nitride in Silicon Photonics 5
- 1.3 Mid-infrared Photonics 6
- 1.4 Outline of the project 6

2 THE DEVICES: RACETRACK RESONATORS, THEIR DESIGN AND FABRICATION 9
- 2.1 Ring and Racetrack Resonators 9
  - 2.1.1 Applications 9
  - 2.1.2 Performance Parameters 10
- 2.2 Post-fabrication Trimming 11
  - 2.2.1 Thermal Tuning 12
  - 2.2.2 Ion Implantation 13
  - 2.2.3 UV and e-beam irradiation 14
- 2.3 Microfabrication 15
  - 2.3.1 Thin-film Formation 15
  - 2.3.2 Photolithography 16
  - 2.3.3 Etching 17
- 2.4 Fabrication of the devices 18
- 2.5 Simulations and selection 21

3 SETUPS AND PROCEDURES 25
- 3.1 Characterisation 25
  - 3.1.1 Setup 25
  - 3.1.2 Procedure 25
- 3.2 Trimming 26
  - 3.2.1 Setup 26
  - 3.2.2 Procedure 27

4 TRIMMING EXPERIMENTS 31
4.1 Preliminary trimming test 31
4.1.1 Results 32
4.2 Final trimming test 33
4.2.1 Dependence on the exposed length 34
4.2.2 Fluence dependence 36

5 SIMULATION OF THE RESONATORS AND THEIR RESPONSE 37
5.1 Design 37
5.2 Results 38
5.2.1 Matching the measurements 38
5.2.2 Effective refractive index 41

6 ANALYSIS OF THE RESULTS 43
6.1 Trimming of the resonant wavelength 43
6.2 Performance Parameters 44
6.3 Thermal stability 45

7 CONCLUSION 47

REFERENCES 49

ACKNOWLEDGMENTS 55

Listing of figures

2.1 All-pass and add-drop configurations of a ring resonator 10
2.2 Simulated resonant wavelength shift due to variations of waveguide width, silicon thickness, and etch depth for a silicon ring resonator [1]. 12
2.3 Waveguide geometry for all the racetrack resonators 18
2.4 Design parameters of a single mode rib waveguide. [2] 19
2.5 Chip layout, with focus on racetrack resonators and normalisation structures. Designed by Thalia Dominguez Bucio (ORC, Southampton). 20
2.6 SEM image of one of the resonators. 20
2.7 2D and 3D views of the simulated device. 21
2.8 Results of the simulation of all the resonator with different configuration . 22

3.1 Setup used for characterising the ring resonators 26
3.2 Example of the behaviour of a straight waveguide with input/output grating couplers. 27
3.3 Setup for laser writing at 244 nm 28
3.4 Schematic of the laser system. 28
3.5 Schematic of the trimming procedure. 29

4.1 Comparison of insertion loss pre and post-exposure (first exposure) 32
4.2 Resonator not affected by laser exposure, before and after laser writing in another area (first exposure) 33
4.3 Resonator on a chip with silicon dioxide cladding, before and after laser writing 34
4.4 Transmission spectra of fabricated racetrack resonators for different lengths of the exposed section of the resonator. a) Device without oxide cladding, b) device with oxide cladding 35
4.5 Dependence of the resonant wavelength shift on the number of lines written on the racetrack. For each line, an arc length of approximately 14 µm has been exposed. a - Device without oxide cladding, b - device with oxide cladding 35
4.6 Shift of the resonant wavelength depending on the fluence. 36

5.1 Design of 2D simulation with FDE monitor. Silicon dioxide in yellow and silicon nitride in light blue. 38

5.2 Real part of the refractive index of nitrogen-rich silicon nitride, measured by ellipsometry up to 1696 nm. 39
5.3 Comparison of the transmission spectra of the simulated and real device. . . 40
5.4 Transmission spectra of the simulated device, before and after changing the refractive index of the silicon nitride layer. 40
5.5 Mode profile obtained with FDE simulation. 41

6.1 Setup used for characterising the ring resonators 45

Listing of tables

6.1 Q factor and extinction ratio calculated before trimming and after writing from to 4 lines on the resonator with oxide cladding. 44

6.2 Q factor and extinction ratio calculated before trimming and after writing from to 4 lines on the resonator without oxide cladding. 44

Light is not so much something that reveals, as it is itself the revelation.

James Turrell

1

Introduction

1.1 SILICON PHOTONICS

Silicon photonics is the branch of photonics that studies the generation, transmission, processing, and detection of light in silicon [3]. Traditionally, interest in this field came from the possibility to integrate photonic devices and optical transmission lines, with electronic components [4]. Silicon photonics, however, has shown much broader potential, thanks to the possible high density of integration and the compatibility with CMOS processes, which allows large production volumes at a low cost; in addition, silicon presents a wide transmission window (even wider if substituted by other compatible materials), it has high thermal conductivity and optical damage threshold, and good nonlinear properties. For example, the Kerr effect is 100 times stronger than in silica fibres, and the Raman effect is even 1000 times larger [4][3].

1.1.1 HISTORY OF SILICON PHOTONICS

The phenomenon of optical guiding in semiconductors was first observed in the 60's, at a GaAs laser p-n junction; from this discovery, other materials and methods to confine light started being investigating, and in 1969, the concept of "Integrated Optics" was introduced by S.E. Miller of Bell's Labs. In his work, he suggested that new devices could be created to manipulate light exploiting surface waveguiding [5] [6].

Regarding silicon-based photonic devices, research in this field dates back to the mid 80's [7], and, in particular, it was in 1985, when the first silicon integrated optical component operating at telecommunications wavelengths was presented [8]. These early researches focused on passive waveguides, active switches and modulators, and they helped to define the fundamental building blocks of silicon photonics devices [3].
Fabrication processes and substrate materials were not yet optimised for this purpose. For this reason, the first silicon-based waveguides yielded very high losses. Once SOI substrates were introduced and, subsequently, Separation by IMplantated OXygen (SIMOX) and Bond and Etch-back SOI (BESOI) fabrcation techniques were developed, these losses quickly decreased; already in 1991, a loss of $0.4\,\mathrm{dB/cm}$ was reported for a silicon rib waveguide, compared to the $15\,\mathrm{dB/cm}$ obtained in 1985 [3][9]. Once the losses started decreasing considerably, the new challenge for waveguide design was miniaturisation, trying to reach sub-micron and nanometric dimensions without considerably increasing losses, which was made possible mainly thanks to the improvements achieved in micro and nanofabrication techniques. At the same time, new materials and configurations were studied, in order to improve the performance of silicon photonics devices and to be able to transmit light at different wavelength windows. Silicon nitride, doped silicon dioxide, silicon oxynitride and polycrystalline silicon, were all employed in fabricating passive devices with different properties from simple silicon-on-insulator [10].

Focusing on waveguides only, was not sufficient, since the complete integration of all the blocks that allow generation, transport and processing of light was one of the first objectives of silicon photonics. It was also necessary to develop other passive devices such as couplers, beam splitters and polarisation rotators, and active devices such as sources, modulators, switches and photodetectors. There are many similarities between the manufacturing of simple waveguides, and other passive devices. Advances in waveguide manufacture generally allowed for advances in the manufacturing of other passive devices. Active devices encountered different issues, mainly due to the indirect bandgap of silicon which makes it difficult to fabricate sources and photodetectors. The solution adopted for creating efficient electrically pumped laser sources and photodetectors was to integrate different group III and V materials on the silicon platform, trying to maintain compatibility with the other integrated devices. [7]
Silicon does not exhibit Pockel elctro-optic effect, which is usually exploited in optical modulators. Since the 80's, however, the possibility of using the free carrier plasma dispersion effect was considered. This effect enables the modulation of the refractive index

of the material, by changing the density of free-carriers in the material. Initially, the modulation rates were in the megahertz range, but more recently, speeds of 90GHz/s have been demonstrated, and the focus moved to the improvement of different performance parameters.

The commercialisation of silicon photonic devices started in the late 90's with sensors and wavelength-divison multiplexing telecommunication products. The dot-com bubble of the early 2000's had a strong negative impact on the first companies that invested in silicon photonics for telecommunications [11]. Despite this initial crisis, many companies kept investing in the research and development of silicon photonic technologies, and their main application nowadays, is in large data centres and high-performance computing companies. These companies are planning to completely replace electrical and multi-mode fibre interconnects with silicon-based interconnects, but some requirements need to be met before this is possible. The cost and the power consumption per data lane of these technologies need to decrease, and they need to become even more reliable and easy to fabricate.[7]

1.2 SILICON NITRIDE IN SILICON PHOTONICS

Silicon nitride is a dielectric material which presents high hardness, thermal shock resistance and chemical stability; all these characteristics, make this material suitable for various applications, mainly as a protective or passivating layer [12].

In addition to its mechanical, electrical and chemical properties, the optical properties of silicon nitride, are the main motivations for its employment in the fabrication of waveguides and waveguide-based devices. Its transparency range extends from 500 nm up to 8.5 µm, reaching wavelengths in the visible where silicon, for example, is absorbing. Therefore, it supports transmission in the near- and mid-infrared, although low loss is achievable only up to 3.7 µm [13][14].

Another advantage of silicon nitride, is the flexibility of its optical properties, which strongly depend on the deposition method. SiN can be either deposited at high temperatures by Low Pressure Chemical Vapour Deposition (LPCVD), or at lower temperature by Plasma Enhanced Chemical Vapour Deposition (PECVD). LPCVD SiN is usually stoichiometric and a good control on the homogeneity and thickness can be obtained. The composition of PECVD SiN, instead, can be tailored to obtain either silicon-rich or nitrogen-rich SiN [15]. The refractive index depends on the composition;

stoichiometric silicon nitride has a refractive index of around 2.00 at 1550 nm, however this value increases for silicon-rich silicon nitride and decreases for nitrogen-rich silicon nitride [16]. The refractive index is always lower than the one of silicon; therefore, the index contrast with a silicon dioxide cladding is also always lower. Because of this property, devices less affected by surface scattering losses, and more tolerant to fabrication errors, can be obtained. However, for equivalent devices, the footprint has to be larger [17].

1.3 Mid-infrared Photonics

The mid-infrared (MIR) region, which includes wavelengths from 2 μm to 20 μm, has been recently considered for photonic applications, and in particular, for communication systems and sensors. This interest comes from the availability of hollow-core photonic bandgap optical fibres with particularly low loss in the 1.9 to 2.1 μm range [ref] and of thulium-doped fibre amplifiers for amplifying the signal [18]. Moreover, several molecules have strong characteristic vibrational transitions in this interval of wavelengths. For this reason, mid-infrared spectroscopy is a suitable tool to identify univocally different molecular species [19].

Mid-infrared applications can be found also for silicon photonics. Silicon and germanium present low loss at these wavelengths [20]. Also, both SOI platforms and silicon nitride are suitable candidates for mid-infrared applications. However, their loss starts increasing considerably at longer wavelengths, so they can only be used around 2 μm [21]. Without considering longer wavelengths, the band from 2 to 5 μm can already enable several applications, from waveguide amplifiers, active imagers, laser radar transceivers, light sources, to secure free-space communications [20]. The main platforms for MIR transmission are silicon nitride, silicon-on-sapphire, suspended silicon, silicon-on-porous silicon, and silicon-germanium-on-silicon [10].

1.4 Outline of the project

The aim of the project is, first, to identify working racetrack resonators on a wafer with a nitrogen-rich silicon nitride layer. To do so the devices are simulated using Lumerical and then the real devices are characterised.

Subsequently, the working devices are exposed to a UV continuous-wave laser. The devices are then characterised again. If the experiment is successful, a shift of the resonant

wavelengths should be observed.
Therefore, in general, the procedure applied to each device is:

1. Characterisation of silicon nitride ring resonators.
2. Exposure of a section of the ring to a laser beam in order to change its refractive index and, consequently, its operating wavelength.
3. Measurement of the exposed devices.

The experiment is then repeated in order to find a dependence of the shift on known parameters.

2

The devices: racetrack resonators, their design and fabrication

The presented project focuses on one of the fundamental blocks of silicon photonics: the ring resonator. Despite its apparent simplicity, this device enables several applications and its properties depend on a large number of factors, which need to be taken into account during its design and fabrication.

2.1 RING AND RACETRACK RESONATORS

A ring resonator is a ring-shaped waveguide, which can couple to one or two other waveguides via codirectional evanescent coupling. If instead of being shaped as a simple circle, the coupling section consists of a straight waveguide, it is called a racetrack resonator. The close loop structure allows a resonance to occur, if the optical path length of the ring or racetrack is equal to $m\lambda$, where m is an integer and λ is the wavelength of the light propagating in the resonator [22].

2.1.1 APPLICATIONS

A simple ring resonator coupled to one waveguide, allows the extraction of a single wavelength from a signal; if another waveguide, also coupled to the resonator, is added, it

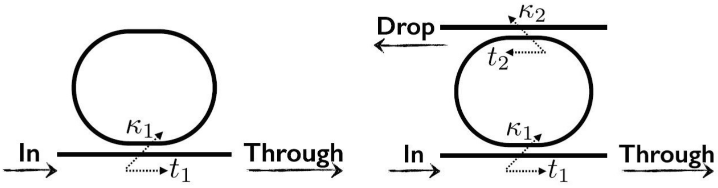

Figure 2.1: All-pass and add-drop configurations of a ring resonator

can function as a drop port, which collects the extracted wavelength. This add-drop configuration (Fig. 2.1), can be employed as a channel dropping filter for wavelength division multiplexed (WDM) signals. [23]

Elctro-optical modulators can also be built if a p-n junction is embedded in the ring resonator [24]. The advantages of using ring resonators instead of Mach-Zender interferometers are mainly the smaller dimension and the lower power consumption. This is due to the fact that, while light travels for many round trips in the ring, it interacts with the carriers multiple times, so less carriers are required to obtain the same results as an MZI [25].

Another important application of ring resonators is in chemical and biochemical sensing. The evanescent field of the light circulating in the resonator can interact with analytes near the surface of the device. The advantage of using ring resonators as sensors, instead of fibres or linear waveguides, is that light circulates for many round trips inside the ring, increasing the effective interaction length. For this reason, ring resonator-based sensors can a have smaller footprint, and require a smaller quantity of analyte. Most ring resonator sensors use a change in the refractive index, which shifts the resonant wavelength, as the sensing mechanism [26].

2.1.2 PERFORMANCE PARAMETERS

The distance between two consecutive resonance peaks is called **free spectral range** (FSR), and it is an important parameter for this type of device, dependent on the length of the resonator. It increases for shorter lengths (which is desirable for many applications), but small devices are more difficult to fabricate and less tolerant to errors [22]. An expression for the FSR can be derived from the resonance wavelength equation:

$$n_{eff} L = m \lambda_r \tag{2.1}$$

where n_{eff} is the effective refractive index, L is the total length of the resonator, and m is an integer. This expression corresponds to:

$$FSR = \frac{\lambda_r^2}{(2\pi R + 2L_c) \cdot n_g} \tag{2.2}$$

where λ_r is the resonance wavelength, R is the radius of the ring, L_c the length of the coupler, and n_g is the group refractive index.

The **quality factor** of a resonator is defined as:

$$Q = \omega \frac{\text{stored energy}}{\text{energy loss}} \tag{2.3}$$

where ω is the angular resonance frequency. For a ring resonator, it measures the sharpness of the resonance peak and can be calculated as follows:

$$Q = \frac{\lambda_0}{\Delta\lambda} \tag{2.4}$$

Which represents the ratio between the resonance wavelength and the 3dB bandwidth [27].

The **extinction ratio** corresponds to the ratio of the maximum output power and the minimum output power. For a ring resonator, the minimum value of the output power is measured when a resonance occurs (if measured from the through port).

$$ER = 10\log_{10}(\frac{P_1}{P_0}) \tag{2.5}$$

This parameter, together with the Q factor, is particularly important when a ring resonator is used as an optical filter; a high extinction ratio and Q factor are, in fact, fundamental for narrow-bandwidth filtering, optical switching and high-sensitivity sensing [28].

2.2 POST-FABRICATION TRIMMING

Ring resonators are small devices, and therefore any fabrication error can lead to significant variations of their operation parameters. All the resonance wavelengths λ_r satisfy the resonance wavelength equation. For this reason, λ_r is dependent on the length, but also on the effective refractive index, which can be strongly affected by fabrication errors. n_{eff} depends, for example, on the waveguide width and the etch depth, but can also vary because of material stress and interface roughness. Figure 2.2 shows an example of how the resonance wavelength shifts with these parameters [29].

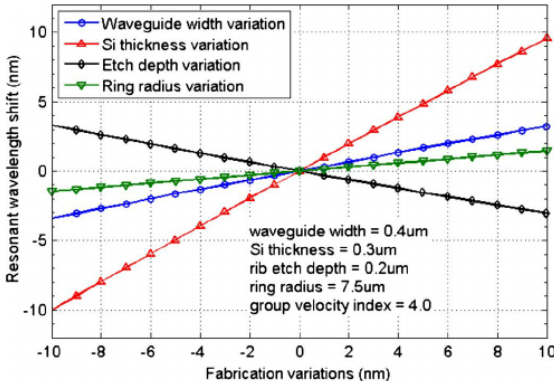

Figure 2.2: Simulated resonant wavelength shift due to variations of waveguide width, silicon thickness, and etch depth for a silicon ring resonator [1].

Therefore, once built, the behaviour of the ring resonator can be much different from the simulated and theoretical one. In order to shift its operative wavelength to the desired one, it is necessary to tune the device. This tuning can involve the whole device or only a section of the ring. In the second case, the resonance wavelength shift as a function of the change of the effective refractive index can be calculated from the following expression [30]:

$$\frac{\Delta\lambda_r}{\lambda_r} = \frac{\Delta n_{\mathit{eff}}}{n_{\mathit{eff}}(\lambda)} \cdot \frac{L_{trim}}{L} \cdot \frac{1}{1 - \frac{\lambda}{n_{\mathit{eff}}(\lambda)} \frac{dn_{\mathit{eff}}}{d\lambda}} \tag{2.6}$$

where $\Delta\lambda_r$ is the resonant wavelength shift, Δn_{eff} is the change in the effective refractive index and L_{trim} is the length of the trimmed section. If many devices are produced at the same time, they need to be individually tested and tuned, and therefore, this operation should be as cheap and fast as possible. Different approaches have been proposed for different materials and applications.

2.2.1 Thermal Tuning

Thermal tuning of the operating wavelength is enabled by the temperature dependence of the effective refractive index. This dependence is measured by the thermo-optic coefficient $\frac{dn}{dT}$ which is a property of the material. Thermal tuning is, therefore, more efficient for materials with a higher thermo-optic coefficient. Polymers, for example, have particularly high thermo-optic coefficients (e.g. $-3.1 \cdot 10^4\,°C^{-1}$ for silicone, $-4.2 \cdot 10^4\,°C^{-1}$ for urethane acrylate elastomer)[31]. Despite these materials being used for fabricating waveguides, other materials like silicon or silicon nitride are preferred, due to their easier integration and compatibility with the CMOS process. Their thermo-optic coefficient is lower, and this increases the power that needs to be provided for tuning. However, it has been demonstrated that the difference in power consumption is not such that this technique is no longer feasible for both silicon and silicon nitride [32][33]. Despite being practically possible to employ this technique, it is usually not ideal. The main drawback to this tuning method is, in fact, that an active heating element must be added and continuously operated and controlled. This can be a particularly critical issue, considering that low power consumption is one of the main achievements of integrated photonic devices. For this reason, an alternative technique would be preferable, especially for passive devices where trimming should be ideally permanent.

2.2.2 Ion Implantation

A permanent change in the resonance wavelength of a ring or racetrack resonator, without needing any additional active device, can be obtained by post-fabrication selective ion implantation.

The implanted ions create deep-level defects which affect the real part of the refractive index, and consequently, the resonance wavelength. In silicon, for example, a resonance shift is observable after implantation. This shift is less pronounced after annealing, because the resonances tend to move towards shorter wavelengths at higher temperature. However, annealing is necessary in order to restore the Q factor of the ring, since with increasing concentration of ion implantation defects, an increase in the optical loss is observable [34]. This post-implantation annealing allows also the tuning of the resonance wavelength, controlling the temperature at which it is performed.

One possible approach is to amorphise silicon in a region of the ring, obtaining a strong change in the refractive index, but at the same time, poor performances and high loss. Alternatively, silicon can be implanted with germanium, and in this case, the implantation dose can be reduced, and with it the processing costs and power consumption. Also, a lower loss and decrease in the Q factor have been observed [35].

2.2.3 UV AND E-BEAM IRRADIATION

Materials such as silicon dioxide, silicon nitride and silicon oxynitride, are all sensitive to UV and e-beam radiations. All these materials, in fact, undergo compaction if exposed to these radiations, causing a variation in the effective refractive index which can be exploited for trimming the resonance wavelength [36]. It is not possible, however, to compact silicon with UV or e-beam irradiation, but this technique can still be employed if the silicon waveguide is built on a SOI platform. In this case it is the oxide which undergoes compaction when exposed to an electron beam; this compaction causes a strain in the silicon lattice and, consequently, an increase in the refractive index and a shift of the resonance to longer wavelengths [36]. It is possible, however, to change its effective refractive index with the amorphisation of the surface of the waveguide, similarly to the ion implantation technique. In this case, no implantation is required, but the resonator is just exposed to femtosecond laser shots. Since even a single shot can be effective, this technique proves particularly fast and simple [37]. Another possible method for trimming silicon ring resonators involves adding a thin film of silicon nitride on top of the silicon waveguide which perturbs the optical mode. The extent of the perturbation depends on the thickness of this layer which can be conveniently etched to shift the resonances [38]. Hydrogenated amorphous silicon resonators can also be effectively tuned simply exposing them to UV laser radiation. In this case, in addition to amorphisation, the change in the refractive index is also due to the dehydrogenation process which is caused by the high temperature reached by the material when exposed [30].

Experiments on silicon nitride ring resonators (vertically coupled in this case) have already been carried out, employing a UV light source with a large spot size (350 μm) that allowed the exposure of the entire ring to the radiation. A maximum trimming range of 12.1 nm and a good stability even after many hours from trimming was obtained [39]. However, the main limitation of this technique is the very long exposure time (up to 6 hours). Alternatively, a photosensitive polymer cladding can be added on top of the silicon nitride layer. Polysilane, in particular, proved to be a suitable polymer for this purpose. The resonance wavelength shift that can be obtained is particularly large (upt to almost 25 nm) and the thermal stability is improved by the polymer layer. However, additional fabrication steps are required and it lacks CMOS compatibility [40].

2.3 MICROFABRICATION

The chips we fabricated were compatible with CMOS process and therefore, microfabrication procedures and techniques were employed. All the possible microfabrication steps can be grouped into four basic operations [41]:

- High-temperature processes to modify the substrate
- Thin-film deposition on the substrate
- Patterning of thin-films and substrates
- Bonding and layer transfer

Each one of these operations can involve several different methods, techniques and materials, depending on the type of device that is fabricated. The main steps for fabricating our chips, in particular, include: thermal oxidation, deposition, photolithography and etching.

2.3.1 THIN-FILM FORMATION

A microfabricated device usually consists of more than one layer of different materials, which can be either grown or deposited on the substrate. The choice of the growth and deposition method depends on the properties of the thin film material which, for example, might or might not be suitable for high temperature treatments, the desired quality and purity of the new layer, and other thin-film characteristics. In general, a thin film can be formed either by thermal oxidation (for silicon dioxide only), doping (for doped silicon layers) or deposition (other materials). A large number of different deposition techniques exist, which can be purely chemical, purely physical, or a combination of the two [42]. Following this distinction, deposition methods can be classified into two main categories: physical vapour deposition (PVD) and chemical vapour deposition (CVD). Each one of these groups contains a large number of different deposition techniques but the most relevant ones are evaporation, molecular beam epitaxy and sputtering, as PVD processes, and low-pressure CVD, plasma-enhanced CVD and atomic layer deposition, as CVD processes [43]:

- *Evaporation* - the material that needs to be deposited is boiled in vacuum; the vapour atoms travel in a straight line and they finally collide on the surface of the chip.

- *Molecular beam epitay (MBE)* - evaporation process performed in ultra-high vacuum, allows to obtain much better control of layer thickness and composition, but it is much slower than simple evaporation.
- *Sputtering* - fast ions hit the target material which atoms are ejected and transported onto the substrate. The target material is placed on the cathode, the substrate is placed on the anode. This process is performed in soft vacuum, and allows excellent adhesion, good uniformity, but it might damage the substrate surface.
- *Low-pressure CVD (LPCVD)* - the substrate is exposed to one or more volatile precursors, which react or decompose on the surface of the substrate. It is performed at a reduced pressure and at high temperature. It can produce layers with good uniformity and good step coverage but its deposition rate is low.
- *Plasma-enhanced CVD (PECVD)* - similar to the previous, but a plasma of the reacting gases is created by an RF, DC or microwave discharge between two electrodes. The deposition temperature can be lower, it is not stoichiometric and the deposited layer could be contaminated by particulate.
- *Atomic layer deposition (ALD)* - self-limited and surface based sequential film growth, which allows atomic scale deposition control. ALD films are conformal and chemically bonded to the surface, however, the extremely slow deposition rate makes it not suitable for layers thicker than 500 nm.

2.3.2 PHOTOLITHOGRAPHY

The photolithography process involves the deposition of a photo-sensitive layer called photoresist, which is exposed and developed in order to form a pattern on the surface of the chip. Some areas of the surface remain covered by the photoresist after the development and they are, therefore, protected from etching, implantation or other pattern transfer mechanisms. Finally, the photoresist is removed. The typical photolithography steps are:

1. Substrate preparation
2. Photoresist spin-coat
3. Post-apply bake
4. Exposure
5. Post-exposure bake
6. Development

7. Postbake

The type of photoresist must be chosen considering the pattern transfer method that will be used, since it needs to be resistant to the chemical or physical agents that will be employed. The exposure can be serial, if a beam of photon, electrons or ions, writes point by point directly on the chip, or it can be parallel if a larger area is exposed to light, using a mask that reproduces the pattern that needs to be transferred. The first is more precise, the latter is much faster [44]. If a mask is used, the minimum pitch (linewidth plus interline space) obtainable can be calculated as follows [45]

$$2b_{min} = 3\sqrt{\frac{\lambda}{n}\left(g + \frac{d}{2}\right)} \tag{2.7}$$

Where $2\mathrm{b}_{\mathrm{min}}$ is the pitch, λ is the wavelength of the exposing light, g is the gap between the mask and the photoresist, and d is the resist thickness and n is the refractive index of the resist. Higher resolution is, therefore, obtainable with a light source with shorter wavelength.

2.3.3 ETCHING

Etching is a pattern transfer mechanism that involves the physical and/or chemical erosion of the areas of the material which are not protected by the patterned photoresist. Etching is usually divided in two classes: wet etching and plasma etching. The basic reaction for wet etching is:

solid + liquid etchant ⇒ soluble products

The basic reaction for plasma etching is instead:

solid + gaseous etchant ⇒ volatile products

Etching involves three main steps: first, transport of etchant to the surface (flow and diffusion), second, surface processes (adsorption, reaction, desorption) and finally removal of product species. Wet etching can take place in a tank where several wafers can be etched at the same time, or alternatively, the etchant can be sprayed on the wafer. It involves either electron transfer (metal etching) or an acid-base reaction (insulator etching). Wet etching usually results in an isotropic etch profile, where the etching front proceeds as a spherical wave, causing undercutting. In some cases, instead, the etchant erodes faster in certain directions, which are related to the crystal planes of the etched material. In plasma etching, the ions in the plasma are accelerated by an RF field to the surface of the wafer. The ions hit the surface vertically, so the etching profile is highly anisotropic. In simple plasma etching, the wafer is on the grounded electrode, while in reactive ion etching (RIE), the wafer is on the biased electrode. In both cases the plasma density and the number of ions that hit the surface cannot be independently controlled. This is possible, instead, with inductively coupled plasma (ICP) etch, where two different RF generators are employed. One maintains the plasma, the other directs the ions towards the wafer, allowing higher process flexibility [41].

2.4 FABRICATION OF THE DEVICES

The rib waveguides and racetrack resonators were fabricated on a nitrogen-rich silicon nitride layer (n = 1.90), which was grown on top of a 3 μm thermally grown SiO_2 layer; the substrate was an 8-inch (200 mm) Si wafer. The SiN layer was deposited by $NH_3 -$ free PECVD at a temperature of 350°C (See [46] for further details). DUV parallel photolithography and ICP etching have been used for patterning. The resulting single mode rib waveguide geometry can be seen on figure2.3; its width is of 1 μm and the etch depth is 0.8 μm.

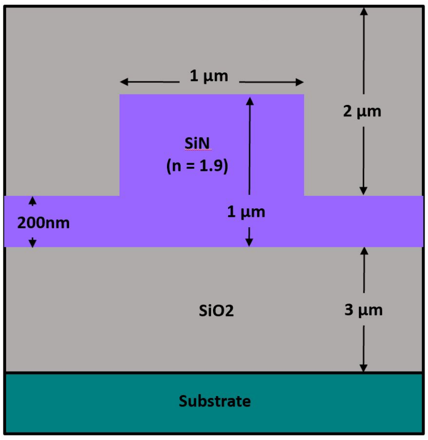

Figure 2.3: Waveguide geometry for all the racetrack resonators

An approximation of the single mode condition valid for quite large rib waveguides (not precise for submicron waveguides) was calculated by Soref *et al.* in 1991 [2]:

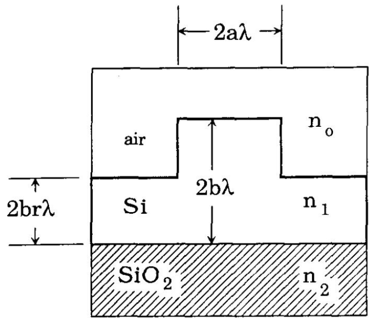

Figure 2.4: Design parameters of a single mode rib waveguide. [2]

$$\frac{a}{b} \leqslant 0.3 + \frac{r}{\sqrt{1-r^2}} \tag{2.8}$$

Where the parameters are defined in Fig. 2.4.
The top silicon dioxide layer is present only in half the chips used for the experiments. Where present, it is 1 μm thick and it was deposited by PECVD at 350°C. This layer serves as cladding but it also allows to compare the results of the application of the proposed laser trimming technique for both types of chips.
The gratings used for coupling light from and to the single-mode fibres used for testing, were optimised for TE polarisation and fabricated with a period of 1470 nm and a target duty cycle of 50% (fabricated 36%). A grating coupler is obtained by periodically changing the refractive index of a region, which can be achieved by material or structural means. For first order diffraction, the period of the grating (Λ) can be calculated setting the free space wavelength λ_{fr} and the off-axis fibre tilt angle θ as follows:

$$\Lambda = \frac{\lambda_{fr}}{n_g - n_{sup/sub} sin\theta} \tag{2.9}$$

Where n_g is the effective grating index and $n_{sup/sub}$ is the refractive index of either the top or bottom cladding [47]. Once fabricated the tilt angle of the fibre might have to be manually adjusted to obtain maximum power, due to possible fabrication imperfections.

The layout of each chip is shown on Fig. 2.5. Each chip contains four arrays of racetrack resonators with four different radii (30, 50, 70 and 90 μm). These arrays include all the possible combinations of straight section length (10, 20, 30, 40, 50 and 60 μm) and gap width (400, 500 and 600 nm), for a total of 18 devices.

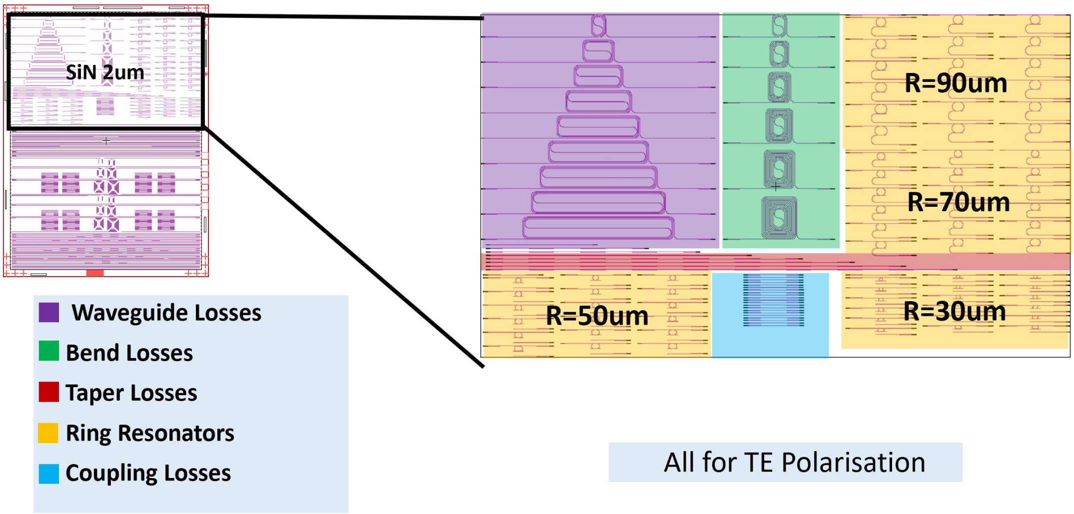

Figure 2.5: Chip layout, with focus on racetrack resonators and normalisation structures. Designed by Thalia Dominguez Bucio (ORC, Southampton).

Figure 2.6 is a scanning electron microscope image of the resulting fabricated devices.

Figure 2.6: SEM image of one of the resonators.

2.5 SIMULATIONS AND SELECTION

N.B. The following convention will be used when labelling devices:
`r`(*radius in* µm)`_l`(*length of the coupler in* µm)`_g`(*gap in* nm)

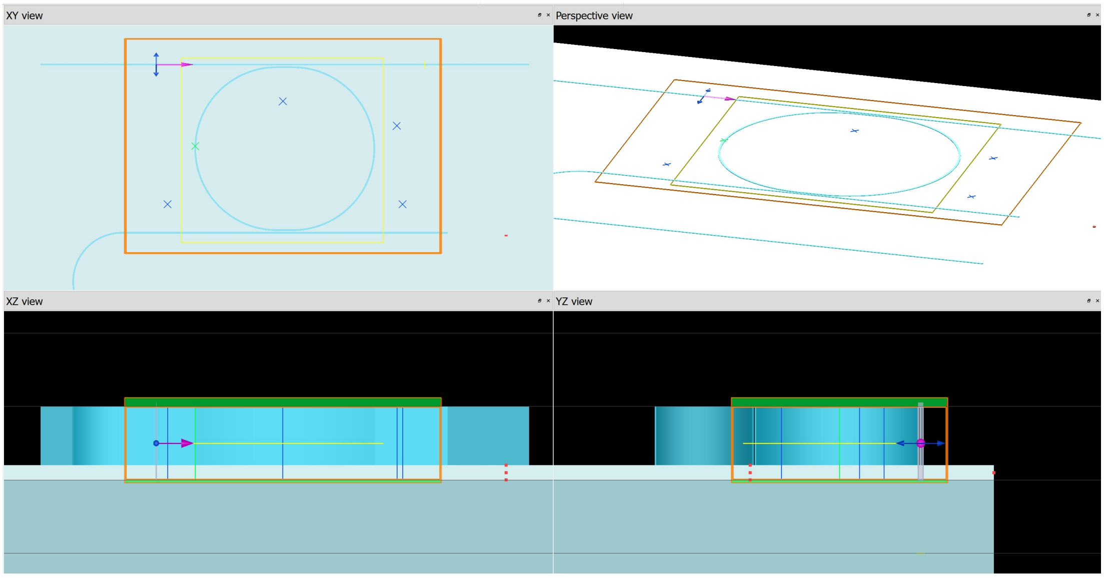

Figure 2.7: 2D and 3D views of the simulated device.

The fabricated devices were simulated using Lumerical MODE Solutions (see chapter 3 for details). All the geometries have been simulated, in order to discard the devices that appeared not to be correctly working. This helped saving time in the laboratory, when the devices with the best performance needed to be selected. In order to simulate the resonance of light in the device, it is necessary to select the variational finite-difference time-domain (FDTD) solver, setting a simulation time that is enough to cover several round trips. In this case the simulation time was of 90 ps. A frequency domain power monitor has been placed at the through port to analyse the transmission spectrum of the resonator. A window from 1940 to 1960 nm has been chosen for the analysis and the resolution was of 500 frequency points in this window. This monitor was just slightly bigger than the waveguide, in order to capture all the optical power going through it. The source had to correspond to the laser source that will be employed in the characterisation of the real devices, and therefore, it needs to be centred at 1.95 µm.

The final design is shown in Figure 2.7; the device is without top oxide cladding, which makes it easier to visualise the structure.

The results of these simulations corresponded to the ideal behaviour of each resonator, which means that the extinction ratio and quality factor of the real resonator are most likely to be lower. Therefore, only the resonators with extinction ratio always greater than 10 dB, and almost always higher than 20 dB could be considered possible candidates. The results of these simulations are summarised in Fig. 2.8; only the resonators corresponding to the green cells were selected and characterised.

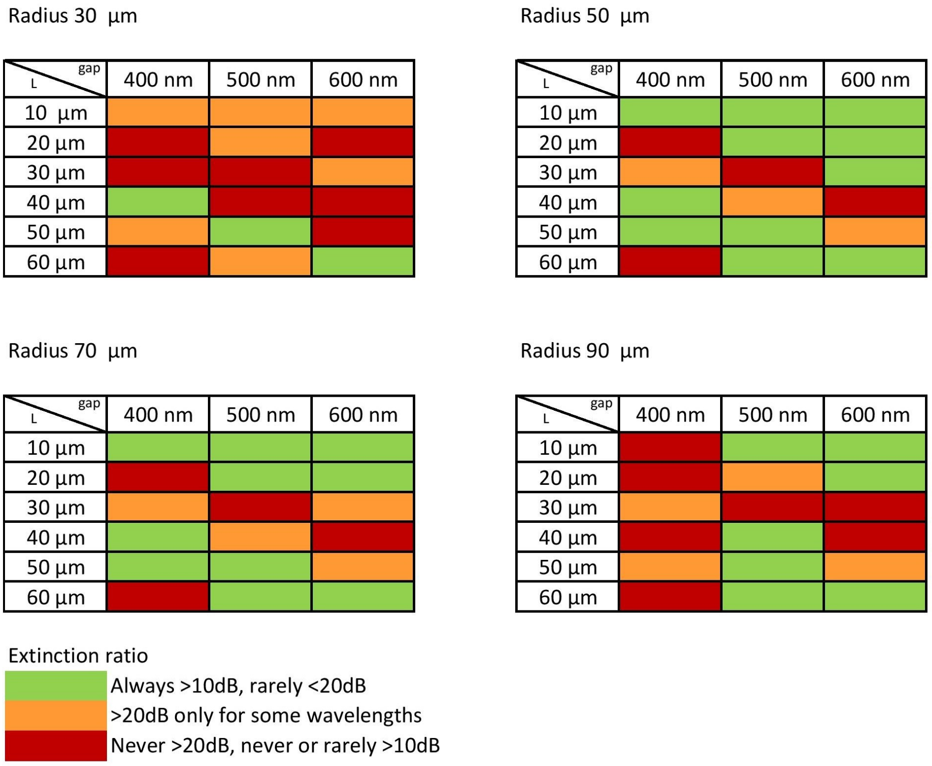

Radius 30 µm

gap L	400 nm	500 nm	600 nm
10 µm	🟧	🟧	🟧
20 µm	🟥	🟧	🟥
30 µm	🟥	🟥	🟧
40 µm	🟩	🟥	🟥
50 µm	🟧	🟩	🟥
60 µm	🟥	🟧	🟩

Radius 50 µm

gap L	400 nm	500 nm	600 nm
10 µm	🟩	🟩	🟩
20 µm	🟥	🟩	🟩
30 µm	🟧	🟥	🟩
40 µm	🟩	🟧	🟥
50 µm	🟩	🟩	🟧
60 µm	🟥	🟩	🟩

Radius 70 µm

gap L	400 nm	500 nm	600 nm
10 µm	🟩	🟩	🟩
20 µm	🟥	🟩	🟩
30 µm	🟧	🟥	🟧
40 µm	🟩	🟧	🟥
50 µm	🟩	🟩	🟧
60 µm	🟥	🟩	🟩

Radius 90 µm

gap L	400 nm	500 nm	600 nm
10 µm	🟥	🟩	🟩
20 µm	🟥	🟧	🟩
30 µm	🟧	🟥	🟥
40 µm	🟥	🟩	🟥
50 µm	🟧	🟩	🟧
60 µm	🟥	🟩	🟩

Extinction ratio

🟩	Always >10dB, rarely <20dB
🟧	>20dB only for some wavelengths
🟥	Never >20dB, never or rarely >10dB

Figure 2.8: Results of the simulation of all the resonator with different configuration

After characterising the selected devices (see Chapter 3 for details), the ones that appeared to have the best performance, were the r50_l10_g500 and r50_l10_g600 resonators, and this was true for all the chips.
The transmission spectrum of the resonators with radius 30 μm was too noisy and the FSR of the devices with radius 70 μm and 90 μm was too small for our purpose. A good compromise was to select resonators with radius 50 μm.

3

Setups and procedures

The experimental work can be divided in two main procedures, that were conveniently modified and repeated in order to obtain the needed results: the characterisation of the devices and their laser trimming.

3.1 CHARACTERISATION

3.1.1 SETUP

The setup used during the characterisation phase is shown in Fig. 3.1

The light is generated by a tunable laser emitting in the wavelength range from 1890 to 2010 nm. Its temperature is stabilised thanks to a temperature controller. The output of the laser enters an optical fibre, which goes through a polariser that maximises the TE/TM ratio, and consequently, the optical power. The fibre is then placed at the correct angle towards the chip, and the same is done for the output fibre, which couples to the output grating coupler. In the end, the collected light reaches a photodetector, which is connected to an oscilloscope and finally, to a computer.

3.1.2 PROCEDURE

First, the angle of the input and output fibres needs to be optimised, so that the output voltage is maximum. The laser has peak power around 1950 nm, therefore, the angle has to

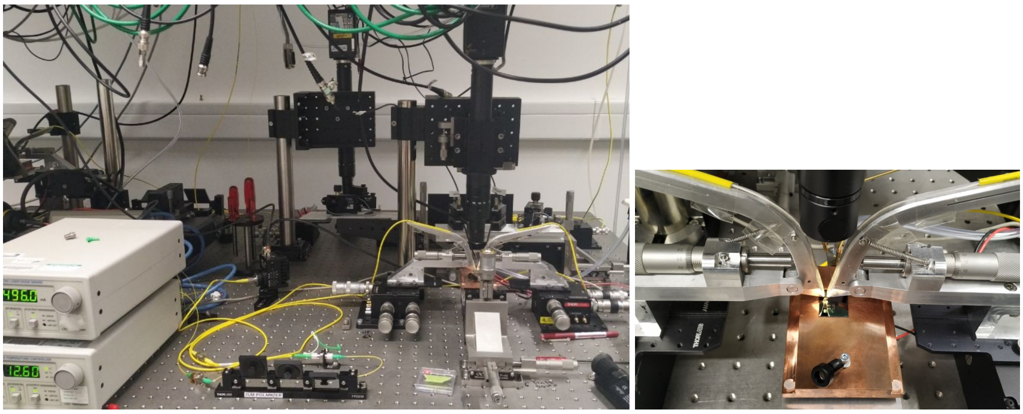

(a) The whole setup

(b) Close-up of the fibres coupling to the devices on the chip

Figure 3.1: Setup used for characterising the ring resonators

be set such that coupling is optimised at the same wavelength. When multiple measurements had to be performed quickly, the angle had to be a trade-off among the optimal ones for different chips.

The chip is then placed under the microscope and the position of the fibres is adjusted to align it to the couplers of the devices. This alignment is completed when the output voltage is maximum. The output can also be increased conveniently moving the polariser.

Finally, the measurement can be performed, and the output voltage is recorded. From this raw data, the insertion loss for each resonator can be calculated, comparing it to a normalisation straight waveguide. This normalisation needs to be performed in order to eliminate the peaks due only to the couplers. Also, the couplers are optimised for a certain wavelength, so the power is lower for wavelengths far from this central wavelength, but this loss is completely independent from the resonators themselves. An example of their behaviour can be observed on Fig. 3.2

3.2 TRIMMING

3.2.1 SETUP

The setup used for trimming is shown on Fig. 3.3 and its main components are schematised in Fig. 3.4. The laser employed for writing on the resonators, is a 244 nm frequency-doubled cw argon-ion laser with spot size of 7 µm. The optical power at the output of the laser is 42 mW, but after crossing the lossy optical system that brings it to the sample, it decreases to

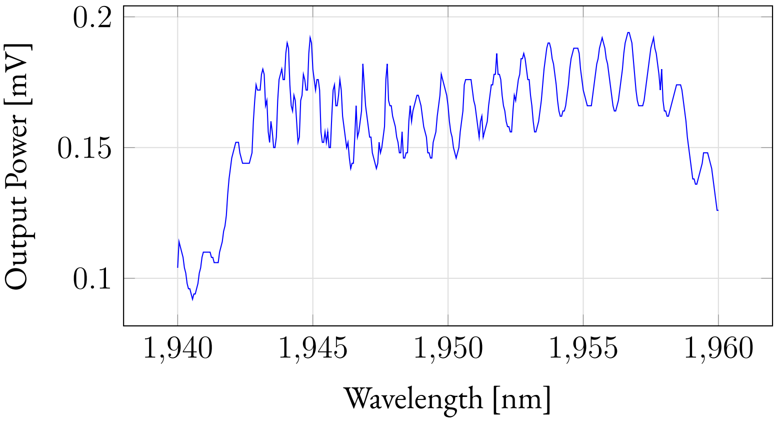

Figure 3.2: Example of the behaviour of a straight waveguide with input/output grating couplers.

25 mV.

The light from the laser is split in two arms by a beam splitter and it recombines on the surface of the sample thanks to a system of mirrors and lenses. Where the two beams recombine, an interference pattern is created and its fringes can be conveniently tuned with an elctro-optical modulator which intercepts one of the two arms. This system is, in fact, usually employed to create Bragg gratings on chips and optical fibres. However, it can also be used to write continuous lines on chips. To do so, the chip needs to move under the laser perpendicularly to the lines of the interference pattern, which, in this way, are no more visible. An example of the application of this setup can be found on [48]. It is not possible, therefore, to write along the racetrack, as it could create undesired patterns. The sample is put on a moving stage that can be both controlled with a joystick (for alignment) and with software (for writing). Another reason why it is not possible to write on the racetrack only, is that the software would have to be completely rewritten.

3.2.2 PROCEDURE

The procedure varies slightly for different experiments, but the main steps are shared. First, the laser needs to stabilise and this can require several minutes, if not an hour. When the output power appears constant ($42 \pm 0.5\text{mW}$), it is possible to use it for exposing the chips. The output power can be maximised moving the frequency-doubling crystal.

At this point, the chip on the moving stage needs to be aligned. The two beams created by the beam splitter, focus on a single point, where the power is maximised. All the four corners of the chip need to be at the same height of this point, in order to obtain a homogeneous

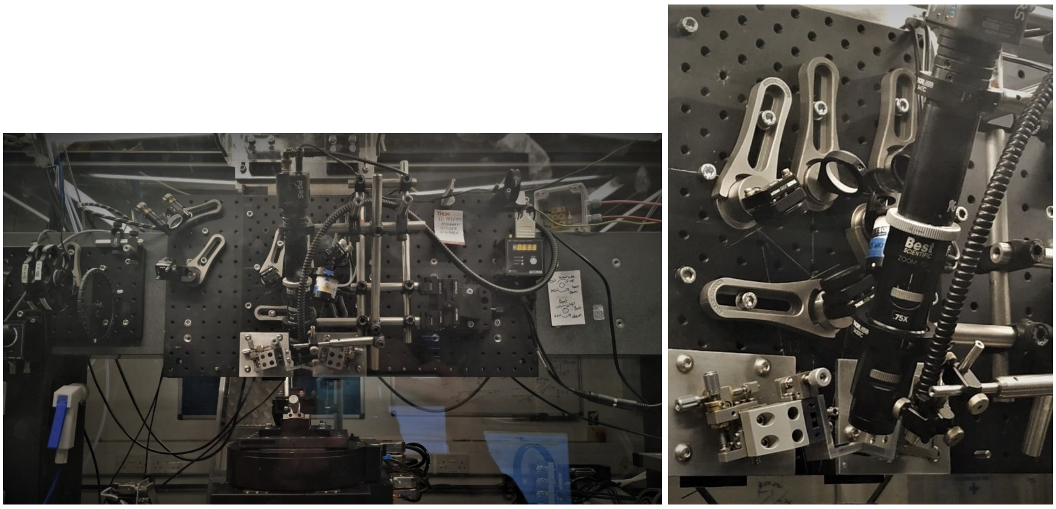

Figure 3.3: Setup for laser writing at 244 nm

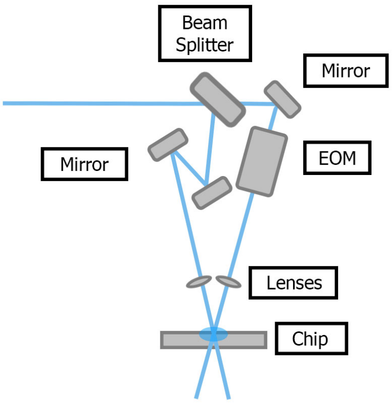

Figure 3.4: Schematic of the laser system.

exposure. Once aligned the chip, it is possible to proceed with the exposure. The starting point is manually set, using a joystick. From that point, the stage is moved automatically with a software (as shown on Fig. 3.5). This setup The software takes as input the number of lines that need to be written, the distance between the lines, the measured optical power that reaches the chip, and the fluence.

The speed at which the stage moves, depends on the set fluence and on the measured optical power of the laser. in this way, the amount of energy transferred onto the sample does not depend on the fluctuations of the laser power. Fluence (F) is defined as optical

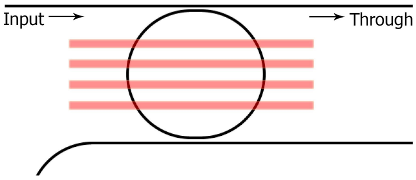

Figure 3.5: Schematic of the trimming procedure.

energy per unit area. The scan speed v is calculated as:

$$v = \frac{2rP_D}{F} \tag{3.1}$$

$$P_D = \frac{P}{\pi r^2} \tag{3.2}$$

Where P_D is the power density, r is the spot radius and P is the optical power of the laser. Considering the parameters of one of the exposures (fluence 40 $\mathrm{kJ/cm^2}$ and laser power 24 mW), the scan speed was 2.73 µm/s. Similar values can be calculated for all the other exposures at the same fluence.

4

Trimming experiments

The exposure of the racetrack resonators to a UV laser beam, and the consequent trimming of the resonance wavelengths, represented the core of the whole project. The feasibility of the proposed technique had to be proven first. Consequently, the exposure was repeated in order to obtain more accurate and significant results.

4.1 PRELIMINARY TRIMMING TEST

The aim of this first exposure with the UV laser was to check if it was possible, using the previously described setup and procedure, to change the refractive index of the material enough to observably shift the resonance wavelength.

At this point the setup was not optimised yet for our purpose and no further data analysis was possible, due mainly to the very coarse alignment. It was not possible, in particular, to know the number of lines written on each resonator. Before aligning the laser to the corner of the chip, we aligned the moving stage employing a similar chip but rich in hydrogen, which enhances its photosensitivity, and makes this operation easier. Once all the four corners of this chip were positioned so that the two laser beams collided in one spot on its surface, we replaced it with the chip with the resonators. We then proceeded with the laser writing; we selected a fluence that we considered high enough, but at the same time that allowed to write at an acceptable speed. The position of the laser was only approximately near the ring, so to make sure that it was hit at least once, we wrote 25 lines in a 1 mm space for the first exposure, and 17 lines in a space of 0.7 mm for the second.

4.1.1 RESULTS

The first test was conducted on the chip without oxide cladding. In this way, the results could not be influenced by any possible absorption occurring in this layer or other factors not dependent on silicon nitride only.

After the exposure, the device was characterised, and its transmission spectrum is shown on Fig. 4.1, compared to the spectrum acquired before the exposure.

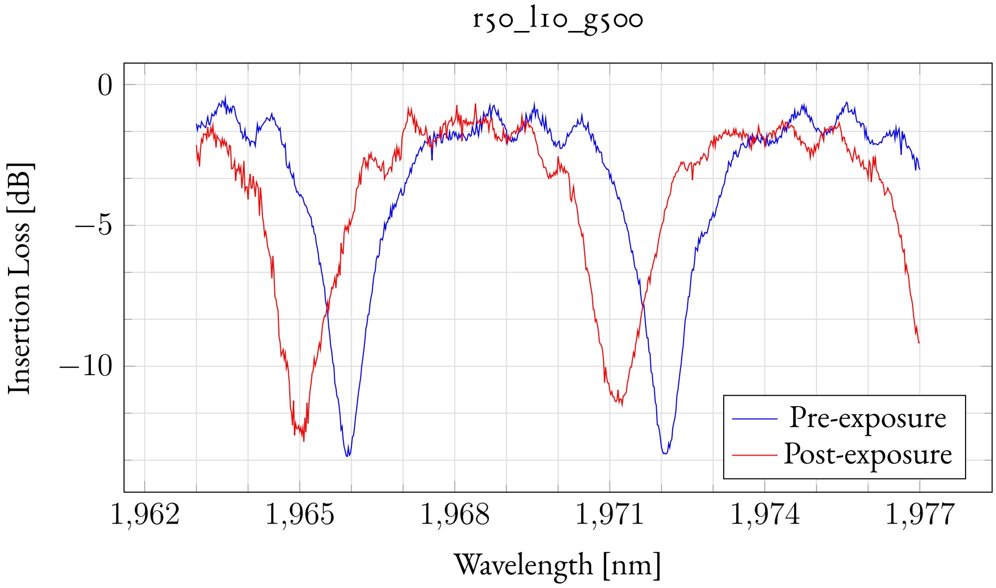

Figure 4.1: Comparison of insertion loss pre and post-exposure (first exposure)

It is possible to observe how the resonance wavelengths indeed shifted towards lower wavelengths, and in particular, the shift is of around 0.9 nm, which is not negligible considering an FSR of around 6 nm.

This means that, despite the change in the refractive index was not immediately visible, it still happened and confirms that it is possible to move the resonance wavelength of a silicon nitride ring resonator with the proposed technique.

To confirm that the shift is not only due to measurement errors, another ring has been remeasured; this resonator was in an area of the chip far from the one hit by the laser. The results are shown on Fig. 4.2. In this case the position of the resonances did not change, meaning that the shift of the previous case was due only to the exposition to the UV laser.

In both cases, the sharpness of the minima is degraded after the laser writing. Since only one of them was actually exposed, this can be due to the measurement setup itself; during the measurements, in fact, it was not possible to obtain the same voltages of the pre-exposure measurements and the results seem more unstable. For this reason, for further experiments, the pre and post-exposure measurements should be performed closer in time and without moving or using the setup for other purposes.

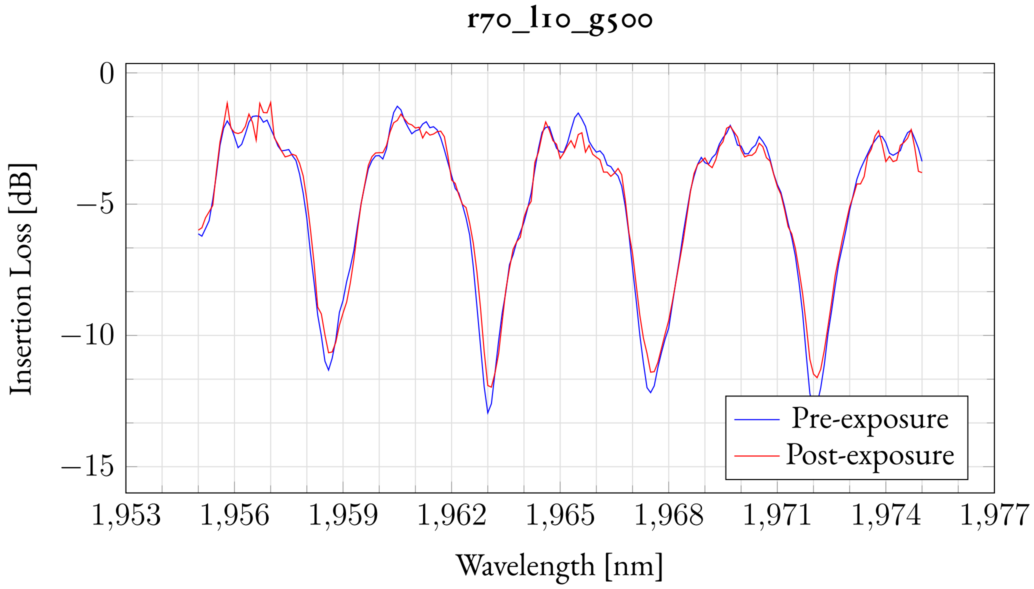

Figure 4.2: Resonator not affected by laser exposure, before and after laser writing in another area (first exposure)

The same procedure has been applied to a chip with a 1 μm thick silicon dioxide cladding. The measured pre and post-exposure transmission spectrum is shown on Fig.4.3.

It is possible to observe how the wavelength moved also in this case, proving that this technique is applicable to silicon-nitride rings both with and without oxide cladding.

4.2 FINAL TRIMMING TEST

The feasibility of the proposed technique has been proven, but in order to make it practically applicable, further experiments had to be carried out. It was necessary to find a relationship between the magnitude of the shift and other parameters. In this way, the resonances can be moved to the target position, appropriately changing the settings of the exposure.

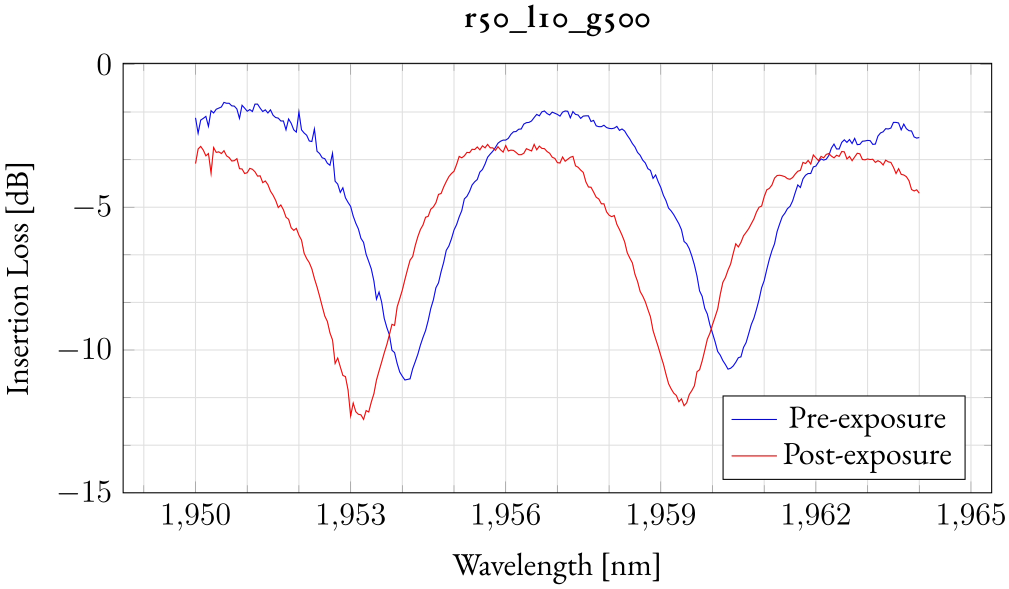

Figure 4.3: Resonator on a chip with silicon dioxide cladding, before and after laser writing

4.2.1 Dependence on the exposed length

From equation 1.6, it is possible to observe how the shift of the resonant wavelength depends on the length of the exposed section of the device. Every time a line is written on the racetrack, two arcs of approximately 7 µm are exposed, for a total length of 14 µm. Therefore, the shift can be controlled changing the number of lines written on the resonator.

In order to observe this dependency, four lines were written on the same resonator, which was characterised after each exposure. It was not possible to write more than four lines on the same device because the point from which the laser started writing could only be moved manually; if this alignment is not correct, the new line might overlap one of the previous lines. The transmission spectra of the trimmed devices, with and without top oxide cladding, compared to the reference device, can be seen in Fig. 4.4

The shift of the resonant wavelengths could be considered linearly dependent on the number of lines and, therefore, to the length of the exposed section, as observable from Figure 4.5.

From the linear dependence it is possible to derive the minimum length that needs to be exposed in order to cover a whole free spectral range (FSR) of 6.15 nm, which, in this case,

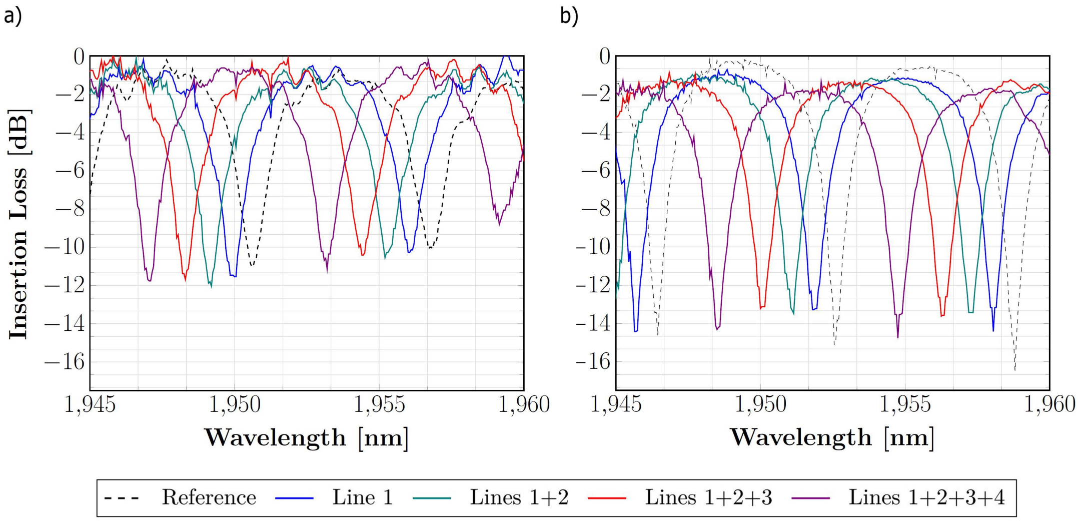

Figure 4.4: Transmission spectra of fabricated racetrack resonators for different lengths of the exposed section of the resonator. a) Device without oxide cladding, b) device with oxide cladding

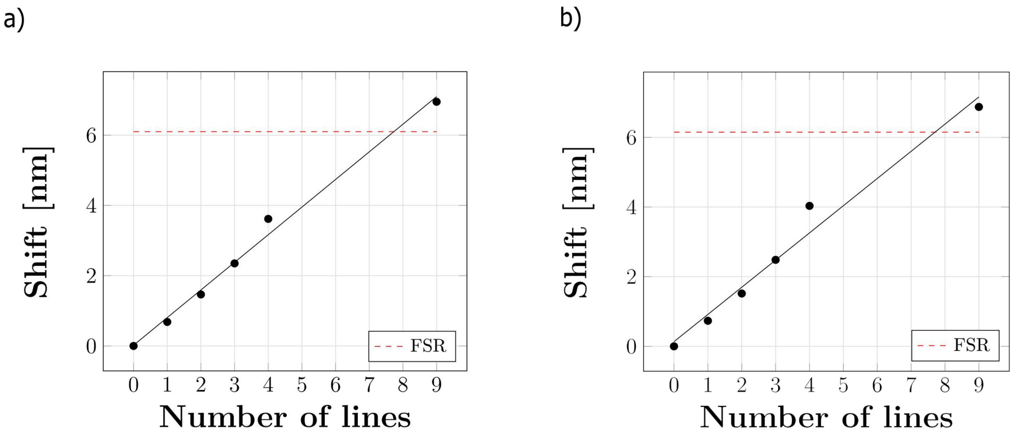

Figure 4.5: Dependence of the resonant wavelength shift on the number of lines written on the racetrack. For each line, an arc length of approximately 14 µm has been exposed. a - Device without oxide cladding, b - device with oxide cladding

is around 106 μm, corresponding to an exposure of 8 lines. We decided to write 9 lines instead (arc length of approximately 126 μm), spacing them of 8 μm, which is only slightly more than the spot size (7 μm), obtaining a shift of 6.95 nm.
This result proves that the device is completely tunable with the proposed technique, independently from how distant the resonant wavelength is, from the target wavelength.

4.2.2 FLUENCE DEPENDENCE

Increasing the fluence, more energy should be transferred into the sample and, therefore, it should be possible to observe a larger shift of the resonant wavelength. For this reason, one line was written on different rings with the same geometry to observe how the shift is affected by the fluence. The results for the devices with top oxide cladding are shown in Fig. 4.6. For practical reasons, it was not possible to have enough points to analyse the trend and the type of dependence but it is possible to affirm that the resonant wavelength shift can be increased by increasing the laser fluence.

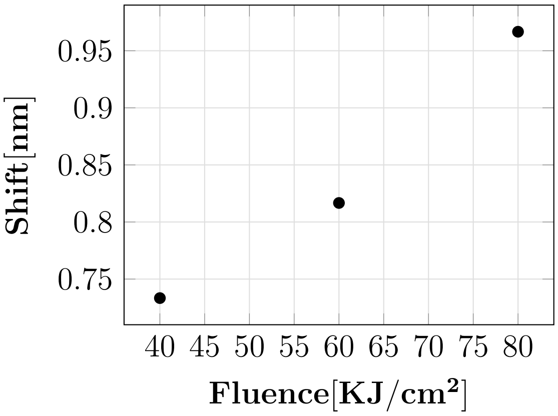

Figure 4.6: Shift of the resonant wavelength depending on the fluence.

5

Simulation of the resonators and their response

The resonators chosen for the final trimming experiment were simulated using Lumeircal MODE Soultions, which is a software specifically created for the simulation of optical fibre systems and integrated photonics [49]. The purpose of these simulations was to match the results obtained with the real devices, in order to be able to calculate some parameters that could not be directly measured.

5.1 Design

The simulated device was the r50_l10_g600, with oxide cladding. The structure was built with the same dimensions as the real device.

Nitrogen-rich silicon nitride is not present in the Lumerical material library and, therefore, the default silicon nitride needs to be customised, changing its refractive index, at least around the wavelength at which the simulation operates.

For the variational FDTD solver, the design and settings were the same as in Section 2.2. In the FDTD method, Maxwell's equations are replaced by a set of finite difference equations [50]. It is a simple ad fast simulation method, and, being a time-domain technique, the response of the system for a wide range of frequencies can be obtained with a single simulation [51].

For these simulations, a finite difference eigenmode (FDE) solver was also added (Fig. 5.1). This solver calculates the spatial profile and frequency dependence of modes, solving Maxwell's equations on a cross-sectional mesh of the waveguide [52]. This monitor allows to observe how the modes are distributed in the waveguide, to calculate their effective refractive index, their group index and check their polarisation ratio (TE/TM).

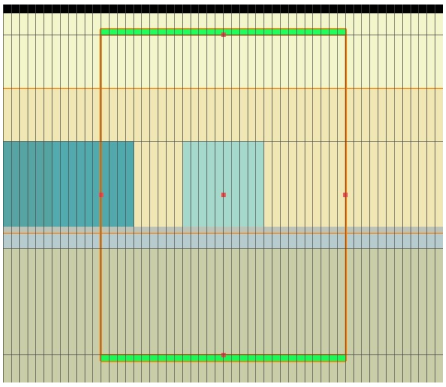

Figure 5.1: Design of 2D simulation with FDE monitor. Silicon dioxide in yellow and silicon nitride in light blue.

5.2 RESULTS

5.2.1 MATCHING THE MEASUREMENTS

The exact refractive index of the nitrogen-rich silicon nitride of the device at 1950 nm was not known. For the first complete simulation with the variational FDTD solver, the refractive index was set as the conventional value for this material at 1550 nm (n = 1.90), which is supposed to be higher than the one at 1950 nm. From the ellipsometry data shown on Fig. 5.2, it can be observed how the refractive index of nitrogen-rich silicon nitride decreases at longer wavelengths. This data was collected at the Optoelectronic Research Centre (Southampton), measuring another chip with nitrogen-rich silicon nitride. Unfortunately, it was not possible to perform the same measurement on our chip and at longer wavelengths.

The obtained transmission spectrum at the through port, had a much shorter FSR than the real case. Knowing that the FSR is inversely proportional to the group refractive index, which is proportional to the refractive index of the material, it was possible to calculate the refractive index necessary to obtain the target FSR. In this case, the needed value for the refractive index of silicon nitride was 1.83.

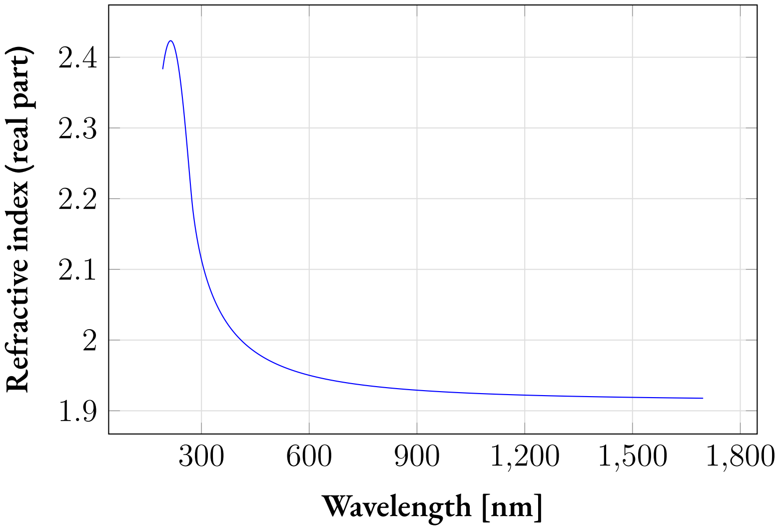

Figure 5.2: Real part of the refractive index of nitrogen-rich silicon nitride, measured by ellipsometry up to 1696 nm.

A simulation was run with these new settings, and the resulting transmission spectrum well matched the measured one, as can be observed from Fig. 5.3.

At this point, the resonant wavelengths had to be shifted of the same amount as the maximum shift obtained from experiments, which was of 6.88 nm for the device with top oxide cladding.

To do so, the refractive index was first changed of an arbitrary amount. Observing the obtained shift, and considering the $\Delta\lambda/\Delta\mathrm{n}$ ratio as constant, the $\Delta\mathrm{n}$ needed to obtain the target resonant wavelength shift was calculated. The calculated value corresponded to $\Delta\mathrm{n} = -0.0067$.

The simulation was run again and the comparison of the new transmission spectra with the previously simulated one is shown in Fig. 5.4.

It is not possible to affirm that the change in the refractive index of silicon nitride in the real device was the same as in the simulations. This is due to the fact that the absorption coefficient for this material, at the wavelength of the laser used for the exposure, is not yet known. This means that, if the light can propagate through the whole thickness of the waveguide, the simulated value would be valid for the real case; if the light is absorbed near the surface, instead, the change in the refractive index could be much higher.

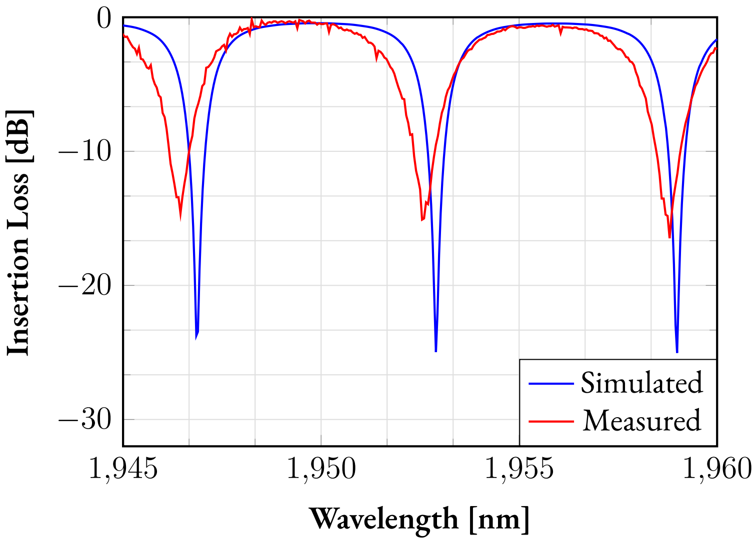

Figure 5.3: Comparison of the transmission spectra of the simulated and real device.

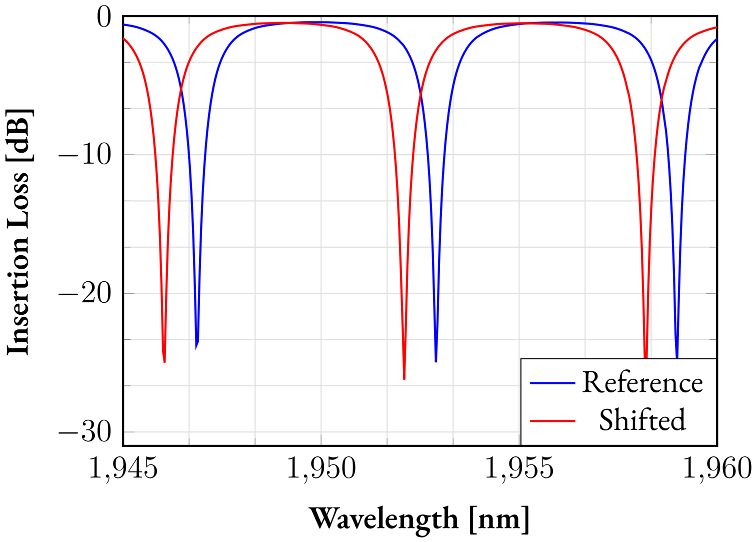

Figure 5.4: Transmission spectra of the simulated device, before and after changing the refractive index of the silicon nitride layer.

5.2.2 Effective refractive index

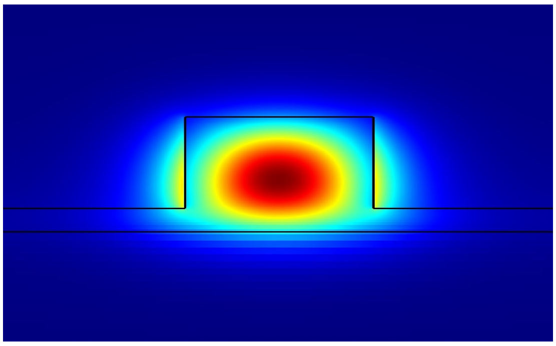

Figure 5.5: Mode profile obtained with FDE simulation.

Instead of referring to the refractive index of the material, it is better to compare the effective refractive index of the fundamental mode; this is a more reliable parameter, since it is related to the propagating mode, not directly to the material itself. To observe how the effective refractive index changes when the shift of the resonant wavelength occurs, it is necessary to run a simulation using the FDE solver, which is also much faster then the FDTD solver. The FDE solver calculates the mode profile for a set number of modes, starting from the fundamental one (effective refractive index closer to the one of the waveguide core). The mode propagating in the real device, being it single mode, is the fundamental TE mode, which needs to be selected among the ones calculated by the solver. This simulation has been run first with the initial value of the refractive index of silicon nitride, and then after matching the resonant wavelength shift, with the new value of the refractive index. The difference between the two values of effective refractive index, before and after the resonant wavelength shift, was of -0.0041. An example of simulated mode profile, can be seen in Figure 5.5.

6

Analysis of the results

In this chapter, the results obtained in the laboratory sessions are analysed, considering how the performance of the device is affected, the possible improvements, and the thermal stability of tuning.

6.1 TRIMMING OF THE RESONANT WAVELENGTH

The experimental results proved that it is possible to shift the resonant wavelength of a nitrogen-rich silicon nitride racetrack resonator, exposing it to a 244 nm laser. The trimmed device had an FSR of 6.15 nm, and the maximum shift obtained was larger than this value (6.88 nm for the device with top oxide cladding, 6.95 nm for the device without top oxide cladding). It is possible to obtain a larger shift with the same technique, if a larger portion of the ring is exposed. This was not practically possible for us, because of our coarse manual alignment.

The device considered had a radius of 50 µm. Being the FSR inversely dependent on the radius of the device, the FSR of a smaller device would be larger. This could represent an issue for obtaining a complete tuning of the resonant wavelength, made worse by the fact that the length of the ring that can be exposed would be shorter. To overcome this problem, it is possible to increase the fluence of the laser, which would increase the resonance shift.

It is interesting to observe how the shift is comparable for the devices with and without top oxide cladding. The slope of the linear dependency of the shift on the length of the exposed section is, in fact, approximately the same. This is due to the fact that silicon dioxide is transparent at 244 nm, which corresponds to the wavelength of the laser used for trimming. However, where the silicon oxide top cladding is present, the optical losses tend to slightly increase after each exposure. This can suggest that an additional strain is created at the interface with the silicon nitride, which could be a potential factor in the change of the refractive index and, consequently, in the resonant wavelength shift. The mechanisms that lead to this change are, however, not yet fully understood. The nitrogen-rich film of the device has a very low concentration of N-N and Si-Si bonds [46]. For this reason, the decrease of the refractive index could be the result of the UV light having enough energy to break Si-H and N-H bonds, releasing hydrogen and allowing the formation of Si-N bonds [53, 54].

6.2 PERFORMANCE PARAMETERS

Some of the proposed techniques compromised the performance parameters of the devices, in particular their Q factor and extinction ratio [34, 35, 36]. It is necessary, therefore, to calculate these parameters for the devices before and after trimming and observe how they change when the shift of the resonant wavelengths increases. Q factor and extinction ratio were calculated for the transmission spectra measured after writing each of the four lines on both devices with and without top oxide cladding (Table 6.1 and 6.2 respectively).

Nr. of lines	0	1	2	3	4
Q factor	1114	1098	1147	1085	1096
Extinction ratio [dB]	-14.86	-13.85	-13.85	-13.61	-14.19

Table 6.1: Q factor and extinction ratio calculated before trimming and after writing from to 4 lines on the resonator with oxide cladding.

Nr. of lines	0	1	2	3	4
Q factor	962	817	756	831	934
Extinction ratio [dB]	-11.75	-11.78	-12.56	-12.19	-11.66

Table 6.2: Q factor and extinction ratio calculated before trimming and after writing from to 4 lines on the resonator without oxide cladding.

In both cases, the performance parameters fluctuated around the same values after trimming, without showing any distinctive trend. This means that the Q factor and the extinction ratio are not observably affected by the exposure to the laser and, therefore, the losses are not increased.

The same parameters were calculated for the results of the simulation described in the previous chapter. For the simulated device with oxide, the Q factor was measured to be approximately 1700 and the extinction ratio of the resonance close to 25 dB. For the samples without oxide cladding the Q factor was measured to be almost 5000 and the extinction ratio varied between 20 dB and 30 dB. Of course, the performance of the simulated devices is much better compared to the real devices, which are affected by fabrication errors, surface roughness and material losses.

6.3 THERMAL STABILITY

The thermo-optic effect determines the change in the refractive index of a material, due to a temperature variation. [55] Since the position of the resonances of a racetrack resonator, depends on the refractive index of the material, this effect needs to be taken into account. For this reason, the resonators have been characterised at different temperatures, recording the position of one of the resonance peaks, positioned around 1955 nm. The results of the measurements are shown on Fig. 6.1

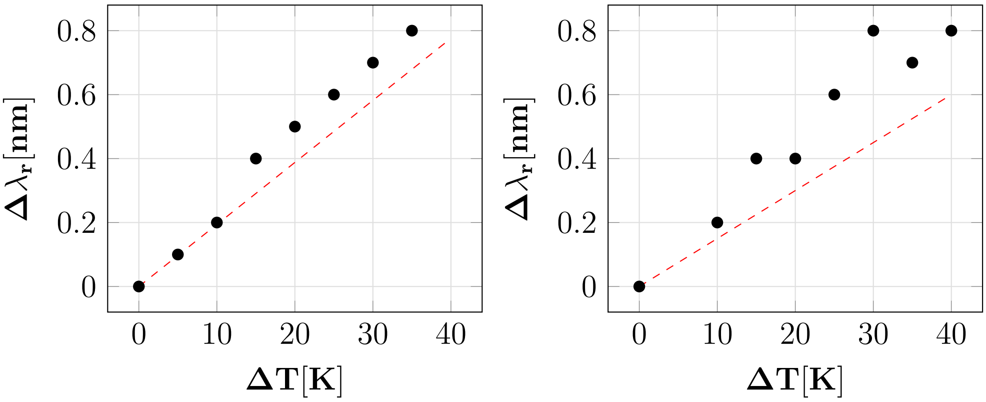

(a) Device with top oxide cladding.

(b) Device without top oxide cladding.

Figure 6.1: Setup used for characterising the ring resonators

The shift per Kelvin measured for the device without top oxide cladding was of 22.0 pm/K; for the device with top oxide cladding was, instead, of 23.6 pm/K. From these values ($\frac{d\lambda_{res}}{dT}$), it is possible to calculate the effective thermo-optic coefficient ($\frac{dn_{eff}}{dT}$), using the formula presented in [56]:

$$\frac{d\lambda_r}{dT} = \frac{\lambda_r}{n_{eff}} \cdot \frac{dn_{eff}}{dT} + \lambda_r \cdot \alpha_{sub} \tag{6.1}$$

Where $\alpha_{\text{sub}} = 2.6\text{x}10^{-6}\text{K}^{-1}$ is the thermal expansion coefficient of the silicon substrate, λ_{r} is the resonant wavelength and n_{eff} is the effective refractive index of the mode. The effective refractive index has been found by simulating the mode profile with Lumerical MODE Solution, as described in the previous chapter.
The effective refractive index depends on the refractive indices of the core and the top and bottom cladding, and this dependence can be expressed as follows: [57]

$$n_{eff} = \Gamma \cdot n_{SiN} + (1 - \Gamma) \cdot n_{SiO_2} \tag{6.2}$$

Where Γ is the confinement coefficient.

It is possible, at this point, to calculate the thermo-optic coefficient, from the following equation:

$$\frac{dn_{eff}}{dT} = \frac{d\Gamma}{dT} \cdot n_{SiN} + \frac{d(1-\Gamma)}{dT} \cdot n_{SiO_2} + \Gamma \cdot \frac{dn_{SiN}}{dT} + (1 - \Gamma) \cdot \frac{dn_{SiO2}}{dT} \tag{6.3}$$

The change of the confinement factor with temperature can be neglected, obtaining this final equation:

$$\frac{dn_{eff}}{dT} \approx \Gamma \cdot \frac{dn_{SiN}}{dT} + (1 - \Gamma) \cdot \frac{dn_{SiO2}}{dT} \tag{6.4}$$

The thermo-optic coefficient of silicon dioxide we considered is equal to $1 \cdot 10^{-5}\text{K}^{-1}$. The confinement factor has been derived from simulation of the waveguide, and it is equal to 0.42. The resulting thermo-optic coefficient of nitrogen-rich silicon nitride is $2.23 \cdot 10^{-5}\,\text{K}^{-1}$.

7

Conclusion

It has been proven that it is possible to trim the operating wavelength of a nitrogen-rich silicon nitride ring resonator, by exposing the device to a UV laser beam. This technique, which is non invasive, enables to achieve full tunability through an entire FSR without visibly compromising the performances of the devices. Also, for the first time, a trimming technique has been demonstrated for devices operating in the mid-IR.

Compared to what proposed by Haewia *et al.* [39], this technique results much faster (seconds to few minutes, instead of several hours) and, therefore, less expensive (less time, lower power consumption) and more easily transferable to industrial production. With automated alignment, the laser could write along the racetrack, instead of writing lines, saving time and obtaining a more accurate control of the length of the exposed section and of the shift of the resonance wavelength. The fabricated device can be quickly characterised and, if the wavelength does not correspond to the desired one, a very simple software can calculate the length of the section that needs to be exposed, knowing the fluence of the laser.

This procedure can be applied to both devices with and without silicon dioxide cladding, since silicon dioxide is transparent at the wavelength of the laser used for trimming. The final devices are usually cladded with oxide, so this result is particularly convenient and makes the presented technique more flexible for different applications.

The applicability of this method does not depend on any specific characteristic of a racetrack resonator, and it depends only on the properties of the material the device is made of. Therefore, it can also be used to trim the optical performance of any other nitrogen-rich silicon nitride based device.

No additional polymer cladding is necessary, maintaining CMOS compatibility and avoiding further complex fabrication steps. Every step of the process does not require to be carried out in a cleanroom, which would increase considerably the costs, and it can be performed at room temperature.

References

[1] A. V. Krishnamoorthy, R. Ho, X. Zheng, H. Schwetman, J. Lexau, P. Koka, G. Li, I. Shubin, and J. E. Cunningham, "Computer systems based on silicon photonic interconnects," *Proceedings of the IEEE*, vol. 97, no. 7, pp. 1237–1361, 2009.

[2] R. A. Soref, J. Schmidtchen, and K. Petermann, "Large Single-Mode Rib Waveguides in GeSi-Si and Si-on-SO2," *IEEE Journal of Quantum Electronics*, vol. 27, no. 8, pp. 1971–1974, 1991.

[3] W. N. Ye and Y. Xiong, "Review of silicon photonics : history and recent advances Review of silicon photonics : history and recent advances," vol. 0340, 2013.

[4] B. Jalali and S. Fathpour, "Silicon photonics," *Journal of lightwave technology*, vol. 24, 2006.

[5] A. Yariv, "The Beginnings of Optoelectronic Integrated Circuits — A Personal Perspective," *Journal of lightwave technology*, vol. 26, no. 9, pp. 1172–1175, 2008.

[6] S. E. Miller, "Integrated Optics : An Introduction," *The Bell System Technical Journal*, vol. 48, no. 7, 1969.

[7] D. Thomson, A. Zilkie, J. E. Bowers, and T. Komljenovic, "Roadmap on silicon photonics," *Journal of Optics*, vol. 18, 2016.

[8] R. A. Soref and J. P. Lorenzo, "Single-crystal silicon: a new material for 1.3 and 1.6 μm integrated-optical components," *Electronics Letters*, vol. 21, no. 21, pp. 953–954, 1985.

[9] G. T. Reed, W. R. Headley, and C. E. J. Png, "Silicon photonics : the early years," *Proceedings SPIE*, vol. 5730, no. Optoelectronic Integration on Silicon II, 2005.

[10] X. Chen, M. M. Milosevic, S. Stankovic, S. Reynolds, T. Domínguez Bucío, K. Li, D. J. Thomson, F. Gardes, and G. T. Reed, "The Emergence of Silicon Photonics as

a Flexible Technology Platform," *Proceedings of the IEEE*, vol. 106, no. 12, pp. 2101–2116, 2018.

[11] A. Rickman, "The commercialization of silicon photonics," *Nature Photonics*, vol. 8, no. August, pp. 579–582, 2014.

[12] A. E. Kaloyeros, F. A. Jové, J. Goff, and B. Arkles, "Review—Silicon Nitride and Silicon Nitride-Rich Thin Film Technologies: Trends in Deposition Techniques and Related Applications," *ECS Journal of Solid State Science and Technology*, vol. 6, no. 10, pp. P691–P714, 2017.

[13] C. Sciancalepore, K. Yvind, S. Olivier, S. Malhouitre, X. Letartre, K. Hassan, C. Monat, H. El Dirani, D. Fowler, S. Kerdiles, M. Casale, S. Garcia, M. Pu, Q. Wilmart, A. Kamel, B. Szelag, N. Tyler, L. Oxenløwe, and W. Rabaud, "A Versatile Silicon-Silicon Nitride Photonics Platform for Enhanced Functionalities and Applications," *Applied Sciences*, vol. 9, no. 2, p. 255, 2019.

[14] P. Tai Lin, V. Singh, L. Kimerling, and A. Murthy Agarwal, "Planar silicon nitride mid-infrared devices," *Applied Physics Letters*, vol. 102, no. 25, pp. 1–6, 2013.

[15] A. Rahim, E. Ryckeboer, A. Z. Subramanian, B. Kuyken, A. Dhakal, A. Raza, A. Hermans, M. Muneeb, Y. Li, U. Dave, P. Bienstman, and N. L. Thomas, "Expanding the Silicon Photonics Portfolio With Silicon Nitride Photonic Integrated Circuits," *Journal of Lightwave Technology*, vol. 35, no. 4, pp. 639–649, 2017.

[16] L. Cai, A. Rohatgi, D. Yang, and M. A. El-Sayed, "Effects of rapid thermal anneal on refractive index and hydrogen content of plasma-enhanced chemical vapor deposited silicon nitride films," *Journal of Applied Physics*, vol. 80, no. 9, pp. 5384–5388, 1996.

[17] S. Severi, R. Baets, A. Z. Subramanian, B. Kuyken, P. Helin, D. Van Thourhout, G. Roelkens, N. Le Thomas, P. Bienstman, and S. Clemmen, "Silicon Photonics: silicon nitride versus silicon-on-insulator," p. Th3J.1, 2016.

[18] Z. Li, A. M. Heidt, J. M. O. Daniel, Y. Jung, S. U. Alam, and D. J. Richardson, "Thulium-doped Fiber Amplifier for Optical Communications at 2 μ m Thulium-doped fiber amplifier for optical communications at 2 μm," *Optics Express*, vol. 21, no. 8, 2013.

[19] A. Schliesser, N. Picqué, and T. W. Hänsch, "Mid-infrared frequency combs," *Nature Photonics*, vol. 6, no. 7, pp. 440–449, 2012. [Online]. Available: http://dx.doi.org/10.1038/nphoton.2012.142

[20] R. Soref, "Mid-infrared photonics in silicon and germanium," *Nature Photonics*, vol. 4, no. 8, pp. 495–497, 2010. [Online]. Available: http://dx.doi.org/10.1038/nphoton.2010.171

[21] G. Z. Mashanovich, M. M. Milošević, M. Nedeljkovic, N. Owens, B. Xiong, E. J. Teo, and Y. Hu, "Low loss silicon waveguides for the mid-infrared," *Optics Express*, vol. 19, no. 8, p. 7112, 2011.

[22] W. Bogaerts, P. de Heyn, T. van Vaerenbergh, K. de Vos, S. Kumar Selvaraja, T. Claes, P. Dumon, P. Bienstman, D. van Thourhout, and R. Baets, "Silicon microring resonators," *Laser and Photonics Reviews*, vol. 6, no. 1, pp. 47–73, 2012.

[23] B. E. Little, S. T. Chu, H. A. Haus, J. Foresi, and J. P. Laine, "Microring Resonator Channel Dropping Filters," *Journal of lightwave technology*, vol. 15, no. 6, 1997.

[24] Q. Xu, B. Schmidt, S. Pradhan, and M. Lipson, "Micrometre-scale silicon electro-optic modulator," *Nature*, vol. 435, no. May, pp. 325–327, 2005.

[25] Q. Xu, B. Schmidt, J. Shakya, and M. Lipson, "Cascaded silicon micro-ring modulators for WDM optical interconnection," *Optics Express*, vol. 14, no. 20, pp. 1669–1671, 2006.

[26] Y. Sun and X. Fan, "Optical ring resonators for biochemical and chemical sensing," *Analytical and Bioanalytical Chemistry*, no. 399, pp. 205–211, 2011.

[27] I. Sadegh Amiri, S. E. Alavi, and S. Mahdaliza Idrus, "Soliton coding for secured optical communication link," *SpringerBriefs in Applied Sciences and Technology*, vol. 2, no. 9789812871602, pp. 17–40, 2015.

[28] J. Wu, T. Moein, X. Xu, and D. J. Moss, "Micro-ring resonator quality factor and extinction ratio enhancement via integrated Fabry-Perot cavity," *Conference on Lasers and Electro-Optics Pacific Rim (CLEO-PR)*, no. d, pp. 1–2, 2017.

[29] A. V. Krishnamoorthy, X. Zheng, G. Li, J. Yao, T. Pinguet, A. Mekis, H. Thacker, I. Shubin, Y. Luo, K. Raj, and J. E. Cunningham, "Exploiting CMOS Manufacturing to Reduce Tuning Requirements for Resonant Exploiting CMOS Manufacturing to Reduce Tuning Requirements for," *IEEE Photonics Journal*, vol. 3, no. 3, pp. 567–579, 2011.

[30] T. Lipka, M. Kiepsch, and H. K. Trieu, "Hydrogenated amorphous silicon photonic device trimming by UV-irradiation Abstract :," vol. 22, no. 10, pp. 12 122–12 132, 2014.

[31] Z. Zhang, P. Zhao, P. Lin, and F. Sun, "Thermo-optic coefficients of polymers for optical waveguide applications," vol. 47, pp. 4893–4896, 2006.

[32] R. Amatya, C. W. Holzwarth, M. A. Popovi, F. Gan, H. I. Smith, F. Kärtner, and R. J. Ram, "Low Power Thermal Tuning of Second-order Microring Resonators," pp. 5–6.

[33] P. Dong, W. Qian, H. Liang, R. Shafiiha, D. Feng, G. Li, J. E. Cunningham, A. V. Krishnamoorthy, and M. Asghari, "Thermally tunable silicon racetrack resonators with ultralow tuning power," vol. 18, no. 19, pp. 20 298–20 304, 2010.

[34] J. K. Doylend, D. F. Logan, R. Vafaei, A. P. Knights, L. Chrostowski, J. J. Ackert, and P. E. Jessop, "Defect-mediated resonance shift of silicon-on-insulator racetrack resonators," *Optics Express*, vol. 19, no. 13, p. 11969, 2011.

[35] M. M. Milosevic, X. Chen, W. Cao, A. F. Runge, Y. Franz, C. G. Littlejohns, S. Mailis, A. C. Peacock, D. J. Thomson, and G. T. Reed, "Ion Implantation in Silicon for Trimming the Operating Wavelength of Ring Resonators," *IEEE Journal of Selected Topics in Quantum Electronics*, vol. 24, no. 4, pp. 1–7, 2018.

[36] J. Schrauwen, D. V. Thourhout, and R. Baets, "Trimming of silicon ring resonator by electron beam induced compaction and strain," *Optics Express*, vol. 16, no. 6, pp. 135–137, 2008.

[37] D. Bachman, Z. Chen, R. Fedosejevs, Y. Y. Tsui, and V. Van, "Permanent fine tuning of silicon microring devices by femtosecond laser surface amorphization and ablation," *Optics Express*, vol. 21, no. 9, p. 11048, 2013.

[38] A. H. Atabaki, A. A. Eftekhar, M. Askari, and A. Adibi, "Accurate post-fabrication trimming of ultra-compact resonators on silicon," *2013 IEEE Photonics Conference, IPC 2013*, vol. 21, no. 12, pp. 428–429, 2013.

[39] H. Haeiwa, T. Naganawa, and Y. Kokubun, "Wide Range Center Wavelength Trimming of Vertically Coupled Microring Resonator Filter by Direct UV Irradiation to SiN Ring Core," *IEEE Photonics Technology Letters*, vol. 16, no. 1, pp. 135–137, 2004.

[40] D. K. Sparacin, C.-y. Hong, L. C. Kimerling, J. Michel, J. P. Lock, and K. K. Gleason, "Trimming of microring resonators by photo-oxidation of a plasma-polymerized organosilane cladding material," *Optics Letters*, vol. 30, no. 17, pp. 2251–2253, 2005.

[41] S. Franssila, *Introduction to Microfabrication*, 2nd ed. John Wiley & Sons Inc., 2010.

[42] K. Seshan, *Handbook of Thin-Film Deposition Processes and Techniques - Principles, Methods, Equipment and Applications*, 2nd ed. William Andrew Publishing/Noyes, 2002.

[43] P. M. Martin, *Handbook of Deposition Technologies for Films and Coatings*, 3rd ed. William Andrew Publishing, 2010.

[44] C. Mack, *Fundamental Principles of Optical Lithography: The Science of Microfabrication*. John Wiley & Sons Inc., 2007.

[45] P. M. Dentinger, K. L. Krafcik, K. L. Simison, R. P. Janek, and J. Hachman, "High aspect ratio patterning with a proximity ultraviolet source," *Microelectronic Engineering*, vol. 62, pp. 1001–1007, 2002.

[46] T. Domínguez Bucio, A. Z. Khokhar, C. Lacava, S. Stankovic, G. Z. Mashanovich, P. Petropoulos, and F. Y. Gardes, "Material and optical properties of low-temperature NH 3 -free PECVD SiNx layers for photonic applications," *Journal of Physics D: Applied Physics*, no. 50, 2017.

[47] S. Nambiar, P. Sethi, and S. K. Selvaraja, "Grating-assisted fiber to chip coupling for SOI photonic circuits," *Applied Sciences (Switzerland)*, vol. 8, no. 7, pp. 1–22, 2018.

[48] S. L. Scholl, A. Jantzen, R. H. S. Bannerman, P. C. Gow, D. H. Smith, J. C. Gates, L. J. Boyd, P. G. R. Smith, and C. Holmes, “Thermal approach to classifying sequentially written fiber Bragg gratings,” *Optics Letters*, vol. 44, no. 3, p. 703, 2019.

[49] “Lumerical Software.” [Online]. Available: https://www.lumerical.com

[50] K. S. Yee, “Numerical Solution of Initial Boundary Value Problems Involving Maxwell’s Equations in Isotropic Media,” *IEEE Transactions on Antennas and Propagation*, vol. 14, no. 3, pp. 302–307, 1966.

[51] B. Archambeault, O. M. Ramahi, and C. Brench, “The Finite-Difference Time-Domain Method,” in *EMI/EMC Computational Modeling Handbook*. Boston, MA: Springer, 1998.

[52] “Finite Difference Eigenmode (FDE) solve.” [Online]. Available: https://kb.lumerical.com/solvers{_}finite{_}difference{_}eigenmode.html

[53] J. J. Mei, H. Chen, W. Z. Shen, and H. F. Dekkers, “Optical properties and local bonding configurations of hydrogenated amorphous silicon nitride thin films,” *Journal of Applied Physics*, vol. 100, no. 7, 2006.

[54] I. Parkhomenko, L. Vlasukova, F. Komarov, O. Milchanin, M. Makhavikou, A. Mudryi, V. Zhivulko, J. Żuk, P. Kopyciński, and D. Murzalinov, “Origin of visible photoluminescence from Si-rich and N-rich silicon nitride films,” *Thin Solid Films*, vol. 626, pp. 70–75, 2017.

[55] G. Cocorullo, F. G. Della Corte, I. Rendina, and P. M. Sarro, “Thermo-optic effect exploitation in silicon microstructures,” *Sensors and Actuators, A: Physical*, vol. 71, no. 1-2, pp. 19–26, 1998.

[56] J. Teng, P. Dumon, W. Bogaerts, H. Zhang, X. Jian, M. Zhao, G. Morthier, and R. Baets, “Athermal SOI ring resonators by overlaying a polymer cladding on narrowed waveguides,” *IEEE International Conference on Group IV Photonics GFP*, no. 1, pp. 77–79, 2009.

[57] V. Raghunathan, W. N. Ye, J. Hu, T. Izuhara, J. Michel, and L. Kimerling, “Athermal operation of Silicon waveguides: spectral, second order and footprint dependencies,” *Optics Express*, vol. 18, no. 17, p. 17631, 2010.

Acknowledgments

I would like to thank, my supervisors Frederic Y. Gardes and Milan Milosevic, and everyone else in the Silicon Photonics group at the Optoelectronics Research Centre of the University of Southampton for the help and support during every stage of the project. I would also like to thank, in particular, Thalia Dominguez Bucio for the fabrication details, Senta Jantzen for the information about the laser writing setup, and Ilias Skandalos for the temperature stability measurements.